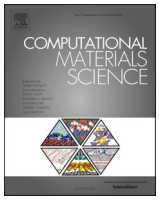
Computational Materials Science 246 (2025) 113367



Contents lists available at ScienceDirect

Computational Materials Science

journal homepage: www.elsevier.com/locate/commatsci



Full Length Article



Molecular dynamics modelling of the stress–strain response of β-sheet nanocrystals

Çetin Taşseven [a,b,1,2,*], Unsal Akdere [b], Seçkin D. Günay [b], Baki Aksakal [b]

[a] Physics, Faculty of Science, University of East Anglia, Norwich Research Park, Norwich NR4 7TJ, United Kingdom
[b] Department of Physics, Faculty of Science and Letter, Yıldız Technical University, Davutpaşa Campus, Istanbul 34210, Turkey

ARTICLE INFO

Keywords:
β-sheet crystals
Molecular dynamics
Stress–strain
Mechanical properties
Hydrogen bonding

ABSTRACT

Molecular dynamics simulations were conducted on two model antiparallel β-sheet crystallites [GA]n and [GAS]n to study deformation in chain, sheet stacking, and hydrogen bonding directions under uniaxial loading. In chain direction, both models were mechanically stable, even beyond the 570 K amorphousation temperature of silk fiber; however, [GA]n model displayed higher yield strain, stress, elastic modulus, and resilience than [GAS]n. In transverse directions, they had similar stress–strain behavior and demonstrated significant anisotropic mechanical behavior. Hence, inclusion of an amino acid with a rich side chain group extending between β-sheets reduces the stiffness of crystallite in chain direction. Serine and alanine residues maintained existing H-bonds and established new ones during stretching in chain direction and shrinking in transverse directions which affected the mechanical response near the yield point. Comparison between β-sheet crystallite and PPTA (Kevlar) showed that the mechanical performance of these crystal polymers were very similar in chain direction, but contrarily β-sheet crystallite had higher stiffness in H-bonding and sheet stacking directions than PPTA. This study may provide a guideline in designing of polyaminoacid based biocompatible materials with superior mechanical performance.

1. Introduction

Bombyx mori silk fibroin (SF) is a semi-crystalline natural polymer and composed of covalently linked heavy-chain (HC) (~350 kDa) and light-chain (~60 kDa) together with P25 (~25 kDa) noncovalently linked to them. The primary structure of HC comprises 12 highly repetitive domains connected with 11 less ordered turs forming the β-sheets with the main amino acid composition of Gly (45.9 %), Ala (30.3 %) Ser (12.1 %) and Try (5.3 %). The unique molecular design of β-sheet crystallites is based on the (Gly-X) dipeptides motif where Ala (~65 %), Ser (~23 %), Try (~12 %) and Val (~5%). The crystallites are embedded into the amorphous region and aligned after the natural spinning process giving the SF a high tensile strength besides the thermal stability, while its great extensibility arising from the amorphous regions [1–4].

The SF has developed advanced distinct functions and properties during the pupa stage of silkworm to provide protection from predators and external conditions. In particular, the extraordinary mechanical properties of the silk fiber outperform most of its biomaterial competitors. Notwithstanding, the molecular composition and design of silk play an important determining role in its mechanical performance, it has not been fully elucidated. Experimentally, it is shown that the size, orientation, and richness of β-sheet crystallites and hydration, and metal infiltration have strong influence on the mechanical performance of the silk fiber. The strength of the spider dragline silk fibers is increased by decreasing the size of the β-sheet crystalline nodes and orienting closed the fiber direction which can be tuned by the reeling speed [5,6]. An applied initial stretch on the fiber results with formation of interlocking regions by the orientation of the crystallites that hinders the cracking at low loads that propagates the force between the adjacent chains [5]. It is suggested that the mechanical properties of Bombyx mori silk can be improved by artificially speeding up the natural spinning of silkworm so that it can be comparable to that of the spider silk [7]. An artificial forcible silking method and differential calorimetry measurement have shown that the tensile properties and the thermal stability of the silkworm silk fiber increased at faster spinning speeds [8]. Dynamic tensile

* Corresponding author.
E-mail addresses: tasseven@yildiz.edu.tr, c.tasseven@uea.ac.uk (Ç. Taşseven).
[1] Present address: Physics, Faculty of Science, University of East Anglia, Norwich Research Park, Norwich NR4 7TJ, United Kingdom.
[2] Permanent address: Department of Physics, Faculty of Science and Letter, Yıldız Technical University, Davutpaşa Campus, Istanbul 34210, Turkey.

https://doi.org/10.1016/j.commatsci.2024.113367
Received 10 May 2024; Received in revised form 6 September 2024; Accepted 8 September 2024
Available online 13 September 2024
0927-0256/© 2024 Elsevier B.V. All rights are reserved, including those for text and data mining, AI training, and similar technologies.

experiments conducted at varying strain rates showed that although strength tends to increase with strain rate, the failure strain of Bombyx mori silk fiber was not significantly impacted by the strain rate [9]. It is reported that hot stretching process increases in the content and orientation of β-sheet nanocrystals of silk fiber which contributes to reinforce the mechanical properties [10]. Elastic modulus of spider Nephila edulis silk decreases with increasing temperature and displayed remarkable toughness and high extensibility below 0°C [11]. In a study on mechanical characteristics and biodegradability of composites biomaterial poly (lactic acid) PLA was found that reinforcement by silk fiber enhances the modulus while decreasing the tensile strength of the composite due to the breakdown of inter- and intramolecular bonding between the silk fiber and PLA during the mixing process [12]. Scanning synchrotron radiation microdiffraction, gel electrophoresis, and mechanical testing experiments under thermal treatment showed that, Bombyx mori silk fiber and β-sheet crystallinity are structurally stable up to 423 K and 500 K, respectively, and the fiber becomes amorphous approximately at 570 K. Both ultimate strain and tensile strength of the SF decrease after about 400 K while the elastic modulus increases up to about 475 K [13].

Molecular dynamics simulations (MD) of models of graphene oxide (GO)-silk nanocomposite [14], carbon nanoscroll (CNS) −silk crystallite [15] and silk fibroin peptide-graphene substrate [16] have established that the mechanical performances of composite, crystallite and silk fibroin can be significantly enhanced arising from their enhanced interactions with graphene and CNS, and H-bond formation with GO. Mechanical response and failure process of silk fiber of silkworm and spider silk have been extensively investigated by molecular dynamics simulations of various molecular models of pure β-sheet crystalline segment [17–22] and combined crystallite and amorphous segments under various mechanical tests [23–30]. Despite that the mechanical response of the β-sheet crystallites against uniform tensile deformation at molecular scale has been overlooked. MD simulations of pull-out test and shear deformation showed that the mechanical performance of crystallites can be improved by nanoconfinement, which is a combination of dissipative molecular stick–slip deformation and uniform shear deformation. The β-sheet crystals with smaller cross-sectional area i.e., smaller number of β-strands, outperform the larger ones in terms of stiffness, strength, and mechanical toughness [20]. Mechanical analysis nanostructure models of Clavipes spider dragline silk constructed as two amorphous domains connected by the terminal residues of a single β-sheet crystallite was also employed using atomistic simulation in order to analyze molecular mechanics and characterize deformation mechanisms [29,30]. Mechanical pull-out test simulations on pure β-sheet crystallites have established that both stick–slip and uniform shear deformations are governed by the hydrogen bonding between the β-strands [19–21] which is hindered by the water content weakening the strength of β-sheets [21]. In addition, the mechanical tensile loading and water concentration effect simulations were performed on four different nanostructure model of Bombyx mory SF developed as each consist of eight β-sheet crystallites connected by amorphous regions [26,27]. Recently, A more realistic atomistic network model of SF with β-sheet crystallites and amorphous domains was developed to investigate the stress distribution of secondary structures of SF during the loading as well as the effect of pre-loading during spinning on mechanical properties [28].

The mechanical behavior of the crystalline and the amorphous region of silk fibroin was independently examined through adapting a model from linear viscoelastic theory to the semicrystalline structure of silk fiber using the combination tensile deformation and x-ray diffraction experiments. It was shown that β-sheet crystallites also contribute the extensibility of silk fiber since they experience elastic deformation in addition to the known multifunctional cross-linking behavior between the amorphous regions [31] The Raman spectroscopy and deformation experiments of silkworm and dragline silk fiber have suggested that both the amorphous region and the crystallites exhibit similar stress but different strain which means they act as in series combination in the fiber under loading [32].

The experimental research on the mechanical characteristics of polymer crystals is not without its difficulties, though. Issues such as the nanometer size scale, sample variability and difficulty of the mechanical tests in transverse to fiber directions make the mechanical measurements on single fibers challenging in experiment [33,34]. Despite several simulation studies on pull-out and shear deformation exist in literature, the underlying mechanism of the mechanical response of the β-sheet crystallites against multiaxial deformation at molecular scale is still not clarified. The mechanical properties of SF are consistently compared in the literature with p-phenylene terephthalamide (PPTA) known as Kevlar, which is a crystalline lattice fiber and suggested as an alternative synthetic material to SF [3,35]. In terms of structural architecture, Kevlar is a crystal lattice fiber and resembles β-sheet crystallite (insets in Fig. 4) sheet [36], but unlike SF which is a composite biomaterial, it lacks disordered amorphous regions where β-sheet crystals are embedded in the form of a cross-linked structure. For that reason, a more accurate approach would be to compare the mechanical properties of β-sheet crystallites and Kevlar due to the similarity of their molecular architecture, rather than silk fibroin. Using various reactive and non-reactive force fields, the MD simulation method was used to study the stress–strain behavior of two polyamide crystallites: PPTA and a related aromatic-aliphatic polyamide derived from a five-carbon aliphatic diacid (PAP5) [33,37].

Thereby, it is desirable and a requisite to study the multiaxial deformation of β-sheet crystallites: (1) to understand the mechanical response at molecular scale; (2) to be able to compare with the materials in the polymer crystal class, such as PPTA and PA, to which β-sheet crystallite also belongs; and (3) to the design of new materials with analogous mechanical properties. In that direction, we aim to investigate the temperature evolution of the stress–strain behavior and the molecular architecture-mechanical behavior relationship in two models of anti-parallel β-sheet crystallites by means of molecular dynamics simulation technique. Firstly, two models of nano-crystallite were constructed by the repetitive unit cells based on the most repeated [Gly-Ala] dipeptide and [Gly-Ala-Gly-Ala-Gly-Ser] hexapeptide motifs. Then, the constant temperature and constant pressure (NPT) simulations were conducted between the temperatures 300 K and 700 K. During heating, the final configuration of crystal structure at the end of each temperature step were subjected to uniaxial deformation at constant rate to determine the stress–strain behavior and mechanical properties of the models.

2. Models and methods

2.1. Construction of crystallites

Two antiparallel β-sheet crystallites models were constructed using the pseudo unit cell space group P_{2_1} and parameters $x = 9.40$ Å (intra-sheet/h-bond direction), $y = 6.97$ Å (chain direction), and $z = 9.20$ Å (inter-sheet/sheet stacking direction) containing eight-amino acid and two anti-parallel β-sheets taken from X-ray diffraction [38]. Using VESTA (Visualization System for Electronic and Structural Analysis) [39] and AVOGADRO [40] software, this initial unit cell then replicated twice along the chain direction to form a new unit cell of four hexapeptide chain in order to accommodate serine residue in one of the models. Finally, nano-crystallites were obtained by replicating the new unit cell twice along sheet stacking and h-bond directions, and once again along the chain direction. The initial size of the nano-crystallites was 2.82 nm, 4.18 nm and 2.76 nm $(3x \times 6y \times 3z)$ formed by 6 anti-parallel β-sheet and 36 polypeptide chains. The detail of the construction is found in elsewhere [41]. Fig. 1 shows the repetitive hexapeptides unit cells $[GA]_{3x2x2}$ and $[GAGAGS]_{1x2x2}$ of the model crystallites, hereinafter referred to as $[GA]_n$ and $[GAS]_n$, respectively.

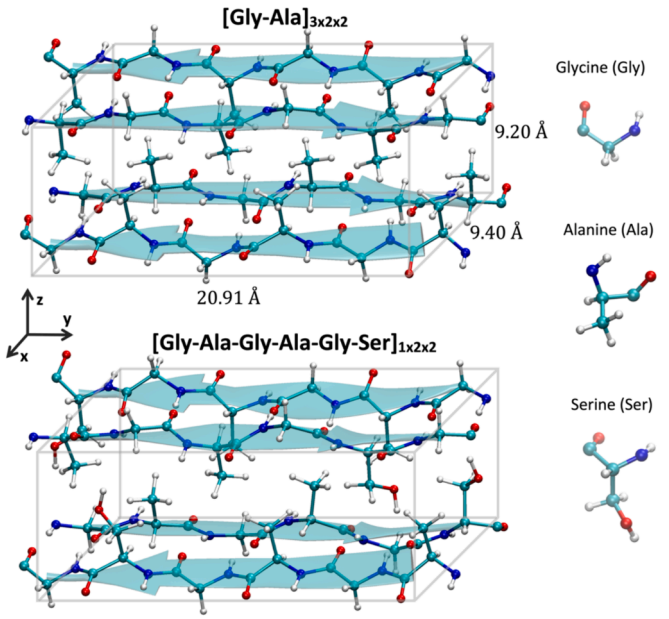


Fig. 1. The unit cells used to construct antiparallel β-sheet crystallites $[GA]_n$ and $[GAS]_n$ The sizes of the cells given here are before the equilibration process. Ball-and-stick model colors corresponds to oxygen, red; nitrogen blue; carbon, cyanide blue; hydrogen, white–gray.

2.2. Molecular dynamics simulation

The MD simulations were performed using GROMACS open-source software [42]. CHARMM 27 force field was used to model the intra-molecular interactions (bonds, angles, dihedrals, impropers and Urey-Bradley) and the inter-molecular interactions (Lennard-Jones and Coulomb) in the nano-crystallites [43]. After the minimization process, the nano-crystallite was equilibrated by performing the constant number, volume, and temperature (NVT) ensemble and the constant number, pressure, and temperature (NPT) ensemble equilibration simulations at $T = 300$ K and $P = 0.1$ MPa. Temperature and pressure were controlled by the velocity rescaling thermostat and Berendsen barostat with temperature coupling parameter 0.1 ps and pressure coupling parameter 2.0 ps, respectively. The Long-range electrostatics interactions were handled with the Particle Mesh Ewald (PME) method. The cut of distance for the non-bonded interactions was 1.2 nm.

Following the equilibration, the isotropic NPT simulation was then conducted at temperatures varying from 300 K up to 700 K with 20 K interval and at $P = 0.1$ MPa. The calculations were carried out for total run time of 50 ns for each temperature with a time step of 0.001 ps. The final configuration of crystal structure at the end of each 40 K temperature step was subjected to uniaxial deformation at constant rate of $\nu = 0.002$nm/ps. The deformation simulations were conducted for 500 ps for each temperature with a time step of 0.0005 ps. During the deformation simulation the isotropic Berendsen barostat was replaced with anisotropic barostat. Consequently, the compressibility in the direction of deformation was set to zero while it was taken as 4.5×10^{-10}pa in the transverse directions. So that, during stretching the crystallite elongates in the deformation direction and shrinks in the perpendicular directions responding to the external pressure. During the deformation simulation the average normal pressure tensor components *Pxx*, *Pyy*, and *Pzz* and the size of the cell (*x*, *y*, *z*) were saved for each 0.05 ps. This was repeated until the desired strain reached (15 %) at each temperature. The periodic boundary conditions are applied in all three directions to replicate the simulation box throughout space. This minimizes the surface effect to form an infinite lattice to minimize the surface effects. The bonding between Carbon atom of carbonyl group (C=O) and Nitrogen atom of amino ($-NH_2$) groups at the terminals of each chain needed to be defined to obtain infinite chain length with no defects.

3. Results and discussions

The aim of the present work is to determine the variation of the axial stress–strain relationship of the anti-parallel β-sheet crystallites with temperature and the effect of serine residue on those. To achieve this, two model nano-crystallites were stretched uniformly in the directions of chain (y-axis) between 300 K-700 K, intra-sheet/hydrogen bonding (x-axis) and inter-sheet/sheet stacking (z-axis) at 300 K using the tools of molecular dynamics simulation.

The equilibrated nano-crystallites were uniaxially stretched at constant rate of $\nu = 0.002$nm/ps beyond up to 15 % strain through successive temperature steps of 40 K from 300 K to 700 K. Fig. 2 shows the stress–strain behavior of β-sheet crystallites of the models $[GA]_n$ and $[GAS]_n$ deformed in the β-strand direction (*y*-axis). To provide a clearer view of the stress–strain behavior at different temperature, the results for 80 K temperature steps are presented in Fig. 2. Both model crystallites exhibit linear stress–strain behavior corresponding to the mathematical model of linear elasticity of solid materials, which is not significantly affected by increasing the temperature, up to the yield point. Estimated value of yield strain and yield stress, respectively, vary approximately in the range of 10.5 %-11.5 % and 36.6GPa-41.2GPa for the crystallite $[GA]_n$, and 9.50 %-9.90 % and 33.1GPa-33.8GPa for $[GAS]_n$ (see also Fig. 3) which lead to difference in resistance and capacity of recovery against elastic deformation between the models. The difference between two models also occurs in the region just around the yield point. The insets in Fig. 2 show the magnified picture of the

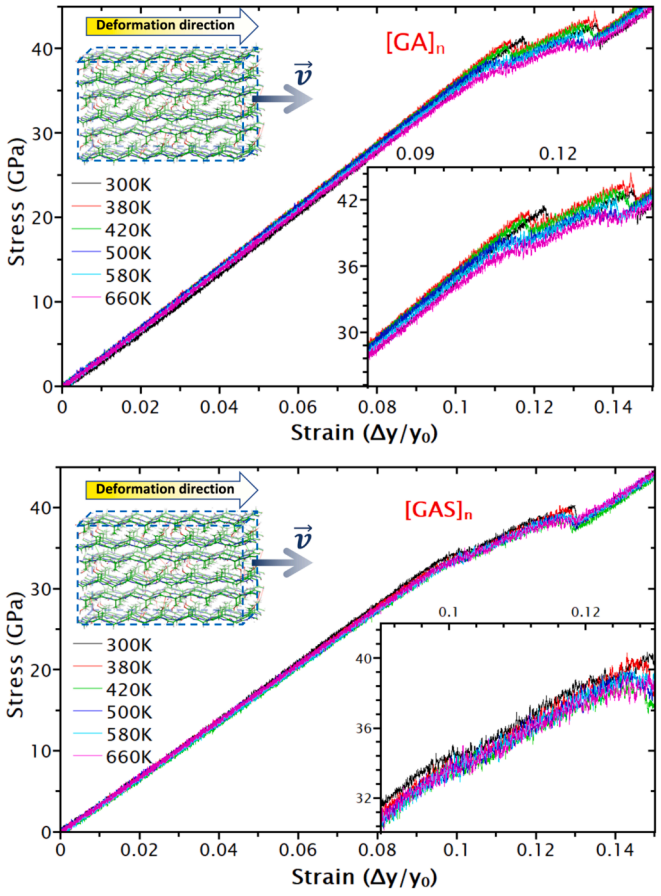


Fig. 2. Stress–strain plots of the two β-sheet crystallites of models $[GA]_n$ and $[GAS]_n$ deformed in the β-strand direction (*y*-axis). For a clearer view the figure was plotted for 80 K temperature steps. The insets are the magnified picture of the stress–strain behavior around the yield point.

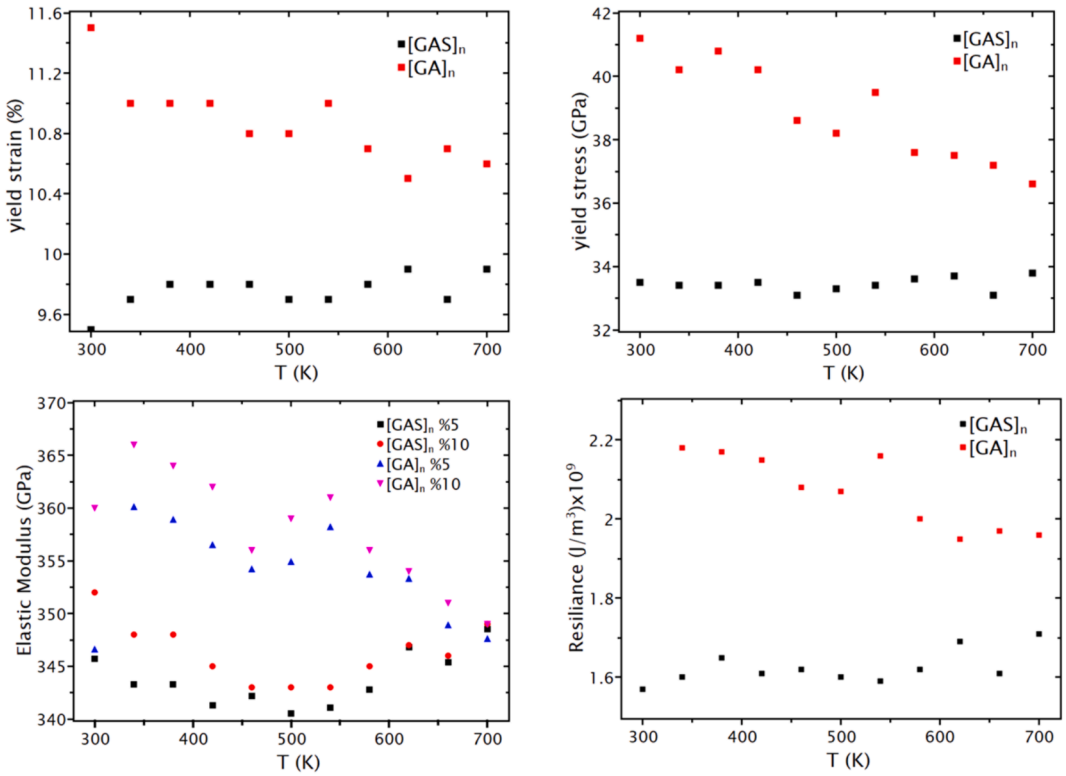


Fig. 3. Temperature dependence of elastic modulus, yield stress, yield strain and resilience of the two β-sheet crystallites of models $[GA]_n$ and $[GAS]_n$ deformed in the β-strand direction (*y*-axis).

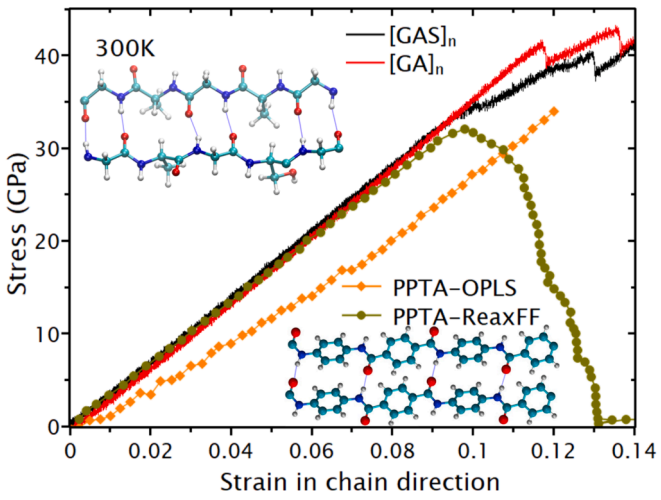


Fig. 4. Comparison between stress–strain curves of $[GA]_n$ and $[GAS]_n$ models of β-sheet crystallites, and polyamide crystallites p-phenylene terephthalamide (PPTA-Kevlar) crystal with nonreactive OPLS [33] and reactive ReaxFF [37] force field in chain direction at 300 K. The insets are the molecular structure of two hexapeptide strand of β-sheet and PPTA.

stress–strain behavior around the yield point. For the $[GAS]_n$ model, a very slow transformation is observed towards a region corresponding pre-rupture regime just before the permanent deformation as the pulling force is increased. Whereas, in the case of $[GA]_n$ model, the transformation takes place with a small sharp drop in strength which is more distinct at low temperature. This mainly arises the hydrogen bonding network and non-bonded interactions as a result of the mutation of one residue from alanine to serine in every hexapeptide. This will be discussed in more detail in the following part of the papers where the corporation of hydrogen bonding is analyzed. As the temperature increased the difference between the models appears to be diminished beyond the 500 K. Also, worth to note that both models are mechanically very stable even at high temperature exceeding the experimentally suggested amorphousation temperature of silk fiber of 570 K.

In Fig. 3, we report the temperature evolution of the mechanical properties, i.e., elastic modulus, yield stress, yield strain and resilience, in the chain direction (*y*-axis). The elastic modulus and the resilience are, respectively, calculated from the slope and the area at the elastic regime of the stress–strain curve. Influence of serine residue on the mechanical properties emerges more clearly in these figures. Inclusion of serine residue evidently reduces all mechanical properties compared to the model constructed by glycine and alanine only. The cross-section area ($A = x \times z$) of the $[GAS]_n$ model perpendicular to the chain direction is about 3 % larger than the cross-section area of $[GA]_n$ after the minimization and equilibration processes of the simulation cells. This arises due to the hydroxyl group (OH) of serine residue extending between the β-sheets that hinders the contraction of the cross-section area of $[GAS]_n$ during the equilibration from being as much as that for $[GA]_n$. The β-sheet crystallite with smaller size can achieve higher resistance and resilience in response to applied load. We also note that all mechanical properties of $[GA]_n$ model slightly decrease as the temperature increases. In contrast, the yield strain, yield strength, and resilience of $[GAS]_n$ model are almost constant while its resistance to elastic deformation slowly reduces up to 500 K then increases as the temperature is increased. Low strain modulus (5 %) is lower than high strain modulus (10 %) which is slightly more significant below 440 K. Overall, hypothetically speaking, all mechanical properties are not significantly affected by the temperature and a small alteration in trend of the behaviors of all properties is noticed around 500 K. This corresponds experimentally reported structural stability temperature of β-sheet crystallinity 500 K [13], provide that considering the fluctuation in temperature is considered in MD calculations.

Kevlar is a syntenic fiber and advanced mechanical performance

arising from its crystalline arrangement which is similar to β-sheet crystallite of silk fibroin. As show in Fig. 4 (inset), the parallel polymer chains of Kevlar, which are formed by the amide linkage of aromatic rings, are held together by hydrogen bonds between the polar amide groups within a Kevlar sheet [36]. This structural arrangement in Kevlar give rise to high tensile strength and thermal stability, as these are provided to SF by the β-sheet crystallites. In the literature, the mechanical properties of SF are always compared with Kevlar as a synthetic alternative [3,35]. However, Kevlar's structural architecture is crystal lattice fiber, and does not have disordered amorphous domains in which the β-sheet crystals embedded in the form of cross-linked configuration that SF has. When a SF in under tensile loading first amorphous domains take the load and become fully uncoiled in the elastic regime and followed by the stretching causing the plastic deformation of SF. Then, the load is transferred to the crystallites enhancing the tensile strength of SF [3,26]. Consequently, instead of silk fibroin, it would be more feasible to compare the mechanical properties of β-sheet crystallites with Kevlar.

The stress–strain behavior of PPTA-Kevlar and PAP5 were studied by the MD simulation method using different types of reactive and non-reactive force fields [33,37]. Stress–strain curves of crystallites $[GA]_n$ and $[GAS]_n$ from our MD simulation at 300 K, and PPTA crystals digitized from Figures 5 and 9 in references [33] and [37], respectively, are presented in Fig. 4. Comparison of the stress strain behavior of model β-sheet crystallites and polyamide crystallites indicates that the similarity in structural arrangement is reflected in mechanical response to uniform tensile load in the elastic region. Tensile modulus, strength, and strain of β-sheet crystallites $[GA]_n$ and $[GAS]_n$ of this work, and PPTA crystals of previous MD simulations using reactive force field ReaxFF [37] and non-reactive force field OPLS [33] at 300 K are given in Table 1. This also shows that the mechanical properties of β-sheet crystallites and PPTA crystal are comparable. Note that, in the pre-rupture region, the β-strands are further stretched and twisted but not to be broken as non-reactive force field CHARMM used here cannot capture peptide bond breaking. Whereas in case of PPTA crystal, where reactive force field has been used, the structural integrity is lost through the breakage of covalent bonds corresponding to nonlinear stress–strain behavior in the pre-rupture regime.

It has been indicated that commercial aromatic polymers, such as aromatic polyamids, polytriphenylamine, polyesters and heterocyclic polymers, which are formed by the incorporation of aromatic segments in polymers, show high thermal stability and mechanical performance. Beside its excellent mechanical strength, the best-known aromatic polymer PPTA-Kevlar has also been reported to exhibit heigh thermal stability with about 700 K decomposition temperature due to its molecular design [33]. Molecular dynamics of stress–strain analysis has shown that the elastic modulus of PPTA crystallite decreases about 8 % from 300 K to 500 K [44], in comparison that is about 2–3 % for the crystallites $[GA]_n$ and $[GAS]_n$ as can be seen in Fig. 3. High thermo-mechanical stability of the crystalline region of p-phenylene benzobisthiazole (PBZT) with constant modulus of 372GPa up to about 673 K has been observed from X-ray diffraction experiments [45]. The elastic moduli of some other polymer crystals such as poly(methylene oxide) (PMO), polyethylene (PE), poly(ethylene terephthalate) (PET), poly (trimethylene terephthalate) (PTT), and poly(butylene terephthalate) (PBT) are 114 GPa, 333 GPa, 182 GPa, 7.1 GPa, and 20.8 GPa, respectively, which have been calculated in the chain direction using density functional theory [46]. The comparison demonstrates that β-sheet crystals $[GA]_n$ and $[GAS]_n$ exhibit high mechanical performance that they outperform their polymer crystal counterparts like PPTA and PBZT crystals.

Table 1
Comparison of mechanical properties elastic modulus, yield strength and yield strain of β-sheet crystallite models and PPTA [33,37] polymer crystals in chain direction at 300 K.

Properties	$[GA]_n$	$[GAS]_n$	PPTA [33]	PPTA [37]
Elastic modulus (GPa)	360	352	362 283 (OPLS)	325
Yield Strength (GPa)	41.2	33.5	34.0	31.9
Yield Strain (%)	11.5	9.5	9.9	9.6

In this part of the work, we focus on the details of the hydrogen bonding network to understand the cooperative behavior of H-bonds between β-strands in the crystalline subjected to tensile deformation. Fig. 5 shows the evaluation of number of H-bonds (total and between Gly-Gly, Ala-Ala, Ser-Ser, Gly-Ala, Ser-Gly, and Ser-Ala pairs) with strain in chain direction at 300 K. Total number of H-bonds of $[GAS]_n$ crystalline is ~ 380 and remains almost constant up to the yield point of ~ 9.5 %. This is about 5 % higher than that of $[GA]_n$ crystallite ~ 365 which slowly decreases to ~ 340 up to the yield point ~ 11.5 %. The additional 15 H-bond in $[GAS]_n$ arises from higher dimensionality of richer side chain hydroxymethyl group (CH_2-OH) of serine residue extending across the sheet-stacking direction compared to side chain methyl group (CH_3) of alanine residue. In addition to dihedral torsional angle (χ_1) around ($C^\alpha - C^\beta$) bond in the side chain of alanine, an extra dihedral angle (χ_2) around (C^β −OH) bond in the side chain of serine increases the configurations of hydrogen bonding. The number of H-bonds between the pair of side chains (Gly-Gly, Ala-Ala, Ser-Ser, Gly-Ala, Ser-Gly, and Ser-Ala) given in Fig. 5 are the accompanying formation of hydrogen bonding in the crystallites across the intra-sheet and inter-sheet directions; H-bonds colored as dark blue dashed line are formed between the adjacent β-strands (intra-sheet direction) on the β-sheet plane and light blue and red colored ones corresponds to H-bons between the neighboring β-sheets (inter-sheet direction). The overall trend of the number of H-bond versus strain is that the H-bonds established by the serine side chain (Ser-Ser, Ser-Gly and Ser-Ala) and between the Ala-Ala pair gradually increase at the elastic region while those established by the glycine sidechain (Gly-Gly and Gly-Ala) clearly decrease. Fig. 6 shows the *xy*, *xz* and *yz* plane view snapshots of the $[GA]_n$ and $[GAS]_n$ models in undeformed state, at 5 % strain, at the yield point and just after the yield point. Change of geometrical form of β-strand, hydrogen bond network and β-sheet structure as a whole is driven by the straightening of backbone, i.e., stretching and bending of covalent bonds and shrinkage of the crystal in the transverse direction as the crystallites elongates in the chain direction during loading.

The results also reveal following important understandings regarding the effect of elongation of β-strands and shrinking along the transverse direction against the 0.1 MPa external pressure during uniaxial loading in the chain direction on the hydrogen bonding network in the crystallites. The ability of glycine amino acid to form hydrogen bonding, who is the only one does not have C^β atom and extended side chain, gradually decreases as the backbone straightens under loading. And the shrinkage along transverse directions (*x* and *z*) falls short to conserve the existing H-bonds or to reform new H-bonds. The alanine and serine amino acids, of which the side chains (CH_3 and CH2-OH) extend between the neighboring β-sheets via C^β atom, are able to conserve the existing H-bonds and establish new bonds due to shrinking β-sheet crystallite transverse directions. A residue with a longer and richer sidechain extending further beyond the backbone in the sheet stacking direction will increase the number of H-bonds. Hence one can expect that this would enhance the strength of crystallite during elastic deformation. But remind that $[GA]_n$ has equilibrated to the smaller cross-section area perpendicular to *y*-axis compared to the $[GAS]_n$ giving rise to a higher mechanical performance. So, it is evident that the extra H-bonding in $[GAS]_n$ remains insufficient to narrow down this difference between the mechanical properties of $[GA]_n$ and $[GAS]_n$ during stretching. In addition to the combination of dissipative molecular stick–slip deformation and shear deformation where the hydrogen bonding plays dominating role at the strain hardening regime during tensile deformation of SF [26], the results of the present study introduce a new case that also needed to be considered when investigating the

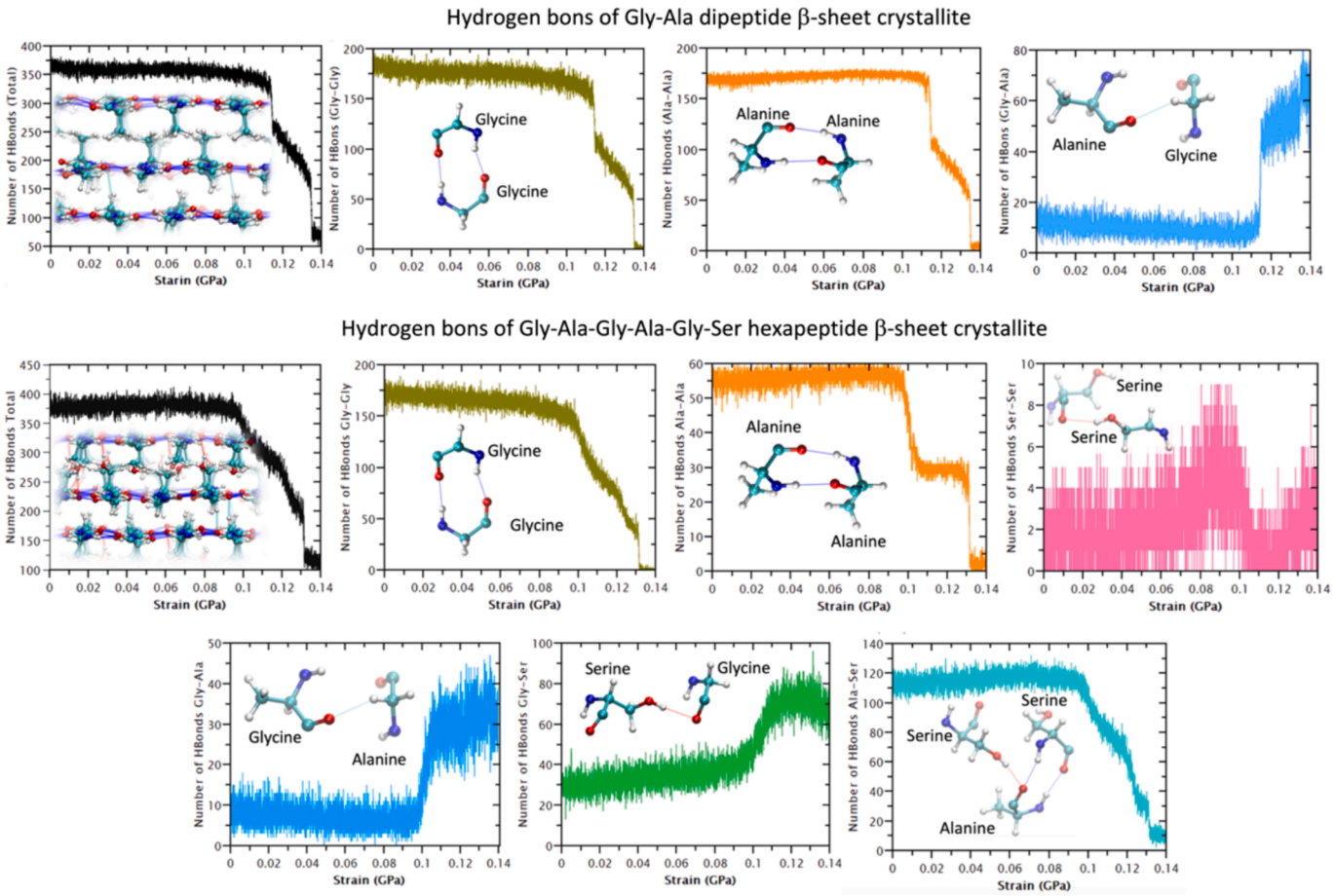


Fig. 5. Evaluation of total number of H-bonds and those established between Gly-Gly, Ala-Ala, Ser-Ser, Gly-Ala, Ser-Gly, and Ser-Ala pairs with strain in chain direction in β-sheet crystallite models at 300 K. The insets are the snapshoots of possible H-bond configurations between the residue pair across the intra-sheet (dark blue dashed lines) and inter-sheet (light blue and red dashed lines) directions.

mechanism of tensile deformation of SF: at the initial stage of strain hardening regime when the crystallites take up the load after the amorphous chains, which are covalently bonded to crystallites, are uncoiled and straightened the variation of H-bonds in crystallites due to stretching in the chain direction and shrinking transversely may also have considerable contribution on the mechanical performance of SF.

In the final part of this study, the stress–strain behavior of $[GA]_n$ and $[GAS]_n$ models of β-sheet crystallites in the transverse directions to *y*-axis (chain direction) *x*-axis (intra-sheet/H-bonding direction) and *z*-axis (inter-sheet/sheet stacking direction) are presented at 300 K. Fig. 7 shows the stress–strain plots for both β-sheet crystallite models crystallites of this work, and PPTA crystals of previous MD simulations [33,37] using reactive force field ReaxFF and non-reactive force field OPLS at 300 K. The OH group of side chain of the serine amino residue extending between the β-sheets in $[GAS]_n$ has no significant contribution and, thus, $[GA]_n$ and $[GAS]_n$ exhibit almost the same response to the strain in the H-bonding and sheet stacking directions. Higher mechanical resistance in the intra sheet direction (*x*-axis) relative to the sheet stacking direction (*z*-axis) is due to the existence of H-bonds rings between the adjacent β-strand. As expected, the mechanical response of β-sheet crystallites is anisotropic like PPTA and determined by the nature of interactions in the corresponding directions.

The elastic modulus crystallites calculated for 2.5 % strain are about 82.0GPa ($[GA]_n$) and 79.0GPa ($[GAS]_n$) in the H-bonding direction, and 38.0GPa ($[GA]_n$) and 41.0GPa ($[GAS]_n$) in the sheet stacking direction. The modulus of PPTA crystal reported in the previous MD simulation studies are 60.0GPa (OPLS) and 74.0GPa. (ReaxFF), and as 8.4GPa (OPLS) and 12.0GPa (ReaxFF) in the directions of H-bonding and π-stacking, respectively. The elastic modulus of some other polymer crystals in the transverse directions have been also reported as 10.9 GPa (PE), 7.2 GPa (PET), 6.9 GPa (PTT), and 4.8 GPa (PBT) in *a* (*x*-axis) direction and 7.8 GPa (PE), 22.3 GPa (PET), 18.4 GPa (PTT), and 11.6 GPa (PBT) in *b* (*y*-axis) direction [46]. This demonstrates that they are also transversely anisotropic, and β-sheet crystallites [GA]n and [GAS]n is mechanically stiffer than aromatic polymer crystals which naturally arises from the existence of the extended side chains between the neighboring sheets and larger number of hydrogen bonds between the adjacent strands in β-sheet crystals compared to polymer crystals. Also note that, mechanical strength and thermal fluctuations are governed by the type of the bonding which are strong covalently bonded interactions in the chain direction, and weak hydrogen bonding network and non-bonded interactions in the transverse directions. This reflected as more pronounced fluctuations in stress–strain curves in the transvers directions compared to the chain direction during deformation simulations.

4. Conclusions

Molecular dynamics simulations of two model β-sheet crystallites constructed by the repetitive sequence of [Gly-Ala] dipeptides and [Gly-Ala-Gly-Ala-Gly-Ser] hexapeptides were carried out to study deformation in the chain direction (*y*-axis), sheet stacking (inter-sheet) direction (*z*-axis) and hydrogen bonding (intra-sheet) direction (*x*-axis) under uniaxial loading at constant rate. The NPT simulations at the temperatures varying between 300 K and 700 K for 40 K temperature step were run prior to stretching the simulation box at constant rate in the chain

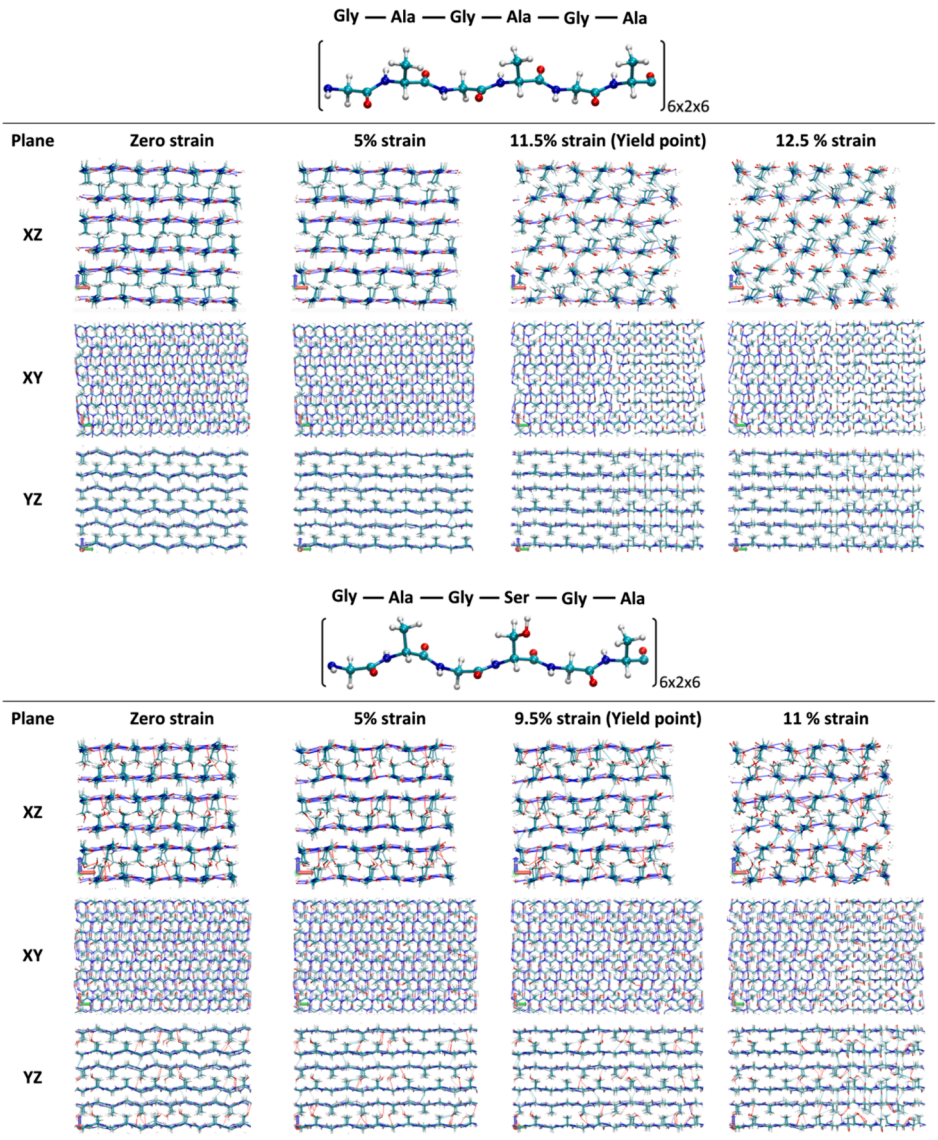


Fig. 6. The *xy*, *xz* and *yz* plane view snapshots of the $[GA]_n$ and $[GAS]_n$ models in undeformed state (zero strain), at 5% strain, at the yield point and after the yield point (see also Supplemantary materials).

direction (*y*-axis) at each temperature. Deformation simulations of the crystallite model in *x* and *z* directions were performed only for 300 K. Anisotropic barostat was used to allow the crystallite to shrink in directions transverse to the applied strain. Mechanical properties were evaluated from the stress–strain curve.

Both $[GA]_n$ and $[GAS]_n$ models of antiparallel β-sheet crystallites under strain in the chain direction are mechanically very stable and almost not effected by the temperature even up to beyond the experimentally suggested amorphousation temperature of silk fiber of 570 K. The mutation from alanine to serine in every three alanine reduces the mechanical properties i.e., yield strain, yield stress, elastic modulus and resilience of $[GAS]_n$ the chain direction. This arises from that the extended hydroxyl group (OH) of serine between neighboring the β-sheets hinders further contraction of $[GAS]_n$ model to the smaller cross-section area perpendicular to *y*-axis during the equilibration process that gives rise to a lower mechanical performance.

Silk fibroin is a semi-crystalline structure composite material consist of β-sheet crystallite domains embedded into amorphous regions. Unlike the comparison made for SF in the literature, in this study we compare the mechanical performance of β-sheet crystallite with that of PPTA (Kevlar), whose molecular architecture are very similar, and both are crystal polymer. The stress strain behavior in the chain direction points out that the elastic response and the mechanical properties of β-sheet crystal akin to that of PPTA crystals. It is shown that β-sheet crystal is also transversely anisotropic due to the difference in nature of interactions, but it exhibits larger elastic resistance than that of PPTA in corresponding H-bonding and sheet stacking directions.

Hydrogen bonding analysis the reveals that the hydroxymethyl (CH_2-OH) and methyl (CH_3) side chain groups of serine and alanine residues extending between the sheets enable them to maintain existing number of H-bonds and establish new ones, albeit small number, during stretching in the chain direction while glycine fails to do this. In addition to stick–slip and shear deformations, this could have considerable effect on resistance at the initial stage of strain hardening regime when the crystallites take up the load after the amorphous chains are uncoiled and straightened.

In summary, this study contributes to our understanding the importance of inclusion of an amino acid with an extended side chain group such as serine for modelling β-sheet crystallite regarding the mechanical response to uniaxial deformation and demonstrates that β-sheet crystallite, but not silk fibroin, can be a comparable polymer crystal to PPTA (Kevlar), contrary to what has been found in the

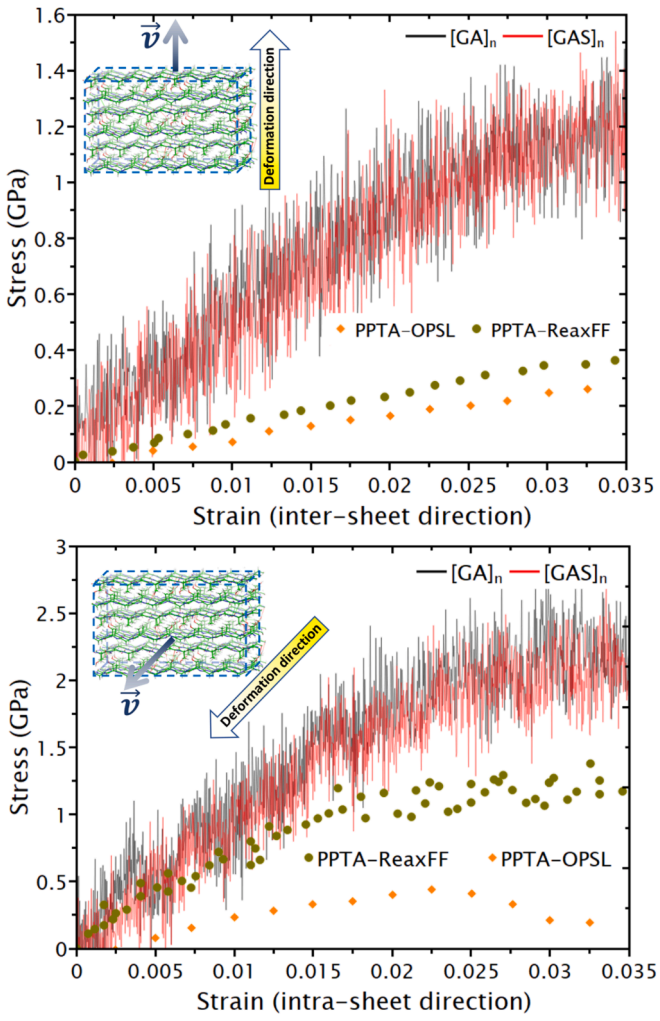


Fig. 7. Stress–strain curves of $[GA]_n$ and $[GAS]_n$ models of β-sheet crystallites, and polyamide crystallites p-phenylene terephthalamide (PPTA) crystal with nonreactive OPLS [33] and reactive ReaxFF [37] force field in x-axis (intra-sheet/H-bonding direction) and z-axis (inter-sheet/sheet stacking direction) at 300 K.

literature so far. The conclusions drawn from the simulations can be informative to the design of new polymer crystal materials with tunable and mechanical properties analogous to β-sheet crystallites.

CRediT authorship contribution statement

Çetin Taşseven: Writing – review & editing, Writing – original draft. **Unsal Akdere:** Methodology. **Seçkin D. Günay:** Methodology. **Baki Aksakal:** Data curation.

Declaration of competing interest

The authors declare that they have no known competing financial interests or personal relationships that could have appeared to influence the work reported in this paper.

Data availability

Data will be made available on request.

Acknowledgments

ÇT gratefully acknowledges the sabbatical support between September 2023 and August 2024 by the Yıldız Technical University and the hosting by the University of East Anglia.

Appendix A. Supplementary material

Video of uniaxial deformation of model β-sheet nanocrystals $[GA]_n$ and $[GAS]_n$ in chain direction.

Supplementary data to this article can be found online at https://doi.org/10.1016/j.commatsci.2024.113367.

References

[1] S. Inoue, K. Tanaka, F. Arisaka, S. Kimura, K. Ohtomo, S. Mizuno, Silk fibroin of bombyx mori is secreted, assembling a high molecular mass elementary unit consisting of H-chain, L-chain, and P25, with a 6: 6 :1 molar ratio, J. Biological Chem. 275 (51) (2000) 40517–40528, https://doi.org/10.1074/jbc.M006897200.
[2] L.D. Koh, Y. Cheng, C.P. Teng, Y.W. Khin, X.J. Loh, S.Y. Tee, M. Low, E. Ye, H. D. Yu, Y.W. Zhang, M.Y. Han, Structures, mechanical properties and applications of silk fibroin materials, Prog. Polym. Sci. 46 (2015) 86–110, https://doi.org/10.1016/j.progpolymsci.2015.02.001.
[3] A. Reizabal, C.M. Costa, L. Pérez-Álvarez, J.L. Vilas-Vilela, S. Lanceros-Méndez, Silk fibroin as sustainable advanced material: material properties and characteristics, processing, and applications, Adv. Funct. Mater. 33 (2023) 2210764, https://doi.org/10.1002/adfm.202210764.
[4] C. Vepari, D.L. Kaplan, Silk as a biomaterial, Prog. Polym. Sci. 32 (8–9) (2007) 991–1007, https://doi.org/10.1016/j.progpolymsci.2007.05.013.
[5] G. Xu, L. Gong, Z. Yang, X.Y. Liu, What makes spider silk fibers so strong? From molecular-crystallite network to hierarchical network structures, Soft Matter 10 (13) (2013) 2116–2123, https://doi.org/10.1039/c3sm52845f.
[6] N. Du, X.Y. Liu, J. Narayanan, L. Li, M.L. Lim, D. Li, Design of superior spider silk: from nanostructure to mechanical properties, Biophys. J . 91 (12) (2006) 4528–4535, https://doi.org/10.1529/biophysj.106.089144.
[7] Z. Shao, F. Vollrath, Surprising strength of silkworm silk, Nature 418 (6899) (2002) 741, https://doi.org/10.1038/418741a.
[8] M.M. Khan, H. Morikawa, Y. Gotoh, M. Miura, Z. Ming, Y. Sato, M. Iwasa, Structural characteristics and properties of Bombyx mori silk fiber obtained by different artificial forcibly silking speeds, Int. J. Biol. Macromol. 42 (3) (2008) 264–270, https://doi.org/10.1016/j.ijbiomac.2007.12.001.
[9] L. Cheng, J. Shao, F. Wang, Z. Li, F. Dai, Strain rate dependent mechanical behavior of B. mori silk, A. assama silk, A. pernyi silk and A. ventricosus spider silk, Materials & Design 195 (2020) 108988, https://doi.org/10.1016/j.matdes.2020.108988.
[10] H. Lu, K. Xia, M. Jian, X. Liang, Z. Yin, M. Zhang, H. Wang, H. Wang, S. Li, Y. Zhang, Mechanically reinforced silkworm silk fiber by hot stretching, Research (Wash D C) (2022), https://doi.org/10.34133/2022/9854063, 9854063.
[11] Y. Yang, X. Chen, Z. Shao, P. Zhou, D. Porter, D.P. Knight, F. Vollrath, Toughness of spider silk at high and low temperatures, Adv. Mater. 17 (1) (2005) 84–88, https://doi.org/10.1002/adma.200400344.
[12] M.P. Ho, K.T. Lau, H. Wang, D. Bhattacharyya, Characteristics of a silk fibre reinforced biodegradable plastic, Compos. Part B: Eng. 42 (2) (2011) 117–122, https://doi.org/10.1016/j.compositesb.2010.10.007.
[13] A. Martel, M. Burghammer, R.J. Davies, C. Riekel, Thermal behavior of bombyx mori silk: evolution of crystalline parameters, molecular structure, and mechanical properties, Biomacromolecules 8 (11) (2007) 3548–3556, https://doi.org/10.1021/bm700935w.
[14] X. Zhou, D. Li, S. Wan, Q. Cheng, B. Ji, In silicon testing of the mechanical properties of graphene oxide-silk nanocomposites, Acta Mechanica 230 (2019) 1413–1425, https://doi.org/10.1007/s00707-017-2017-y.
[15] Y. Cheng, L.-D. Koh, F. Wang, D. Li, B. Ji, J. Yeo, G. Guan, M.-Y. Han, Y.-W. Zhang, Carbon nanoscroll–silk crystallite hybrid structures with controllable hydration and mechanical properties, Nanoscale 9 (26) (2017) 9181–9189, https://doi.org/10.1039/C7NR01428G.
[16] Y. Cheng, L.-D. Koh, D. Li, B. Ji, Y. Zhang, J. Yeo, G. Guan, M.-Y. Han, Y.-W. Zhang, Peptide-graphene interactions enhance the mechanical properties of silk fibroin, ACS Appl. Mater. Interfaces 7 (39) (2015) 21787–21796, https://doi.org/10.1021/acsami.5b05615.
[17] M.J. Buehler, S. Keten, Elasticity, strength and resilience: a comparative study on mechanical signatures of α-Helix, β-sheet and tropocollagen domains, Nano Res. 1 (2008) 63–71, https://doi.org/10.1007/s12274-008-8006-7.
[18] S. Keten, M.J. Buehler, Geometric confinement governs the rupture strength of H-bond assemblies at a critical length scale, Nano Lett. 8 (2) (2008) 743–748, https://doi.org/10.1021/nl0731670.
[19] S. Xiao, W. Stacklies, M. Cetinkaya, B. Markert, F. Gräter, Mechanical response of silk crystalline units from force-distribution analysis, Biophys. J. 96 (10) (2009) 3997–4005, https://doi.org/10.1016/j.bpj.2009.02.052.
[20] S. Keten, Z. Xu, B. Ihle, M.J. Buehler, Nanoconfinement controls stiffness, strength and mechanical toughness of β-sheet crystals in silk, Nature Mater 9 (2010) 359–367, https://doi.org/10.1038/nmat2704.
[21] Y. Cheng, L.-D. Koh, D. Li, B. Ji, M.-Y. Han, Y.-W. Zhang, On the strength of β-sheet crystallites of Bombyx mori silk fibroin, J. R. Soc. Interface 11 (96) (2014) 20140305, https://doi.org/10.1098/rsif.2014.0305.

[22] C. Xu, D. Li, Y. Cheng, M. Lui, Y. Zhang, B. Ji, Pulling out a peptide chain from β-sheet crystallite: propagation of instability of H-bonds under shear force, Acta Mech. Sin. 31 (2015) 416–424, https://doi.org/10.1007/s10409-015-0404-y.
[23] A. Nova, S. Keten, N.M. Pugno, A. Redaelli, M.J. Buehler, Molecular and nanostructural mechanisms of deformation, strength and toughness of spider silk fibrils, Nano Lett. 10 (7) (2010) 2626–2634, https://doi.org/10.1021/nl101341w.
[24] G. Bratzel, M.J. Buehler, Molecular mechanics of silk nanostructures under varied mechanical loading, Biopolymers 97 (6) (2012) 408–417, https://doi.org/10.1002/bip.21729.
[25] M. Cetinkaya, S. Xiao, F. Gräter, Effects of crystallile subunit size on silk fiber mechanics, Soft Matter 7 (2011) 8142–8148, https://doi.org/10.1039/C1SM05470H.
[26] M. Patel, D.K. Dubey, S.P. Singh, Phenomenological models of Bombyx mori silk fibroin and their mechanical behavior using molecular dynamics simulations, Mater. Sci. Eng. 108 (2020) 110414, https://doi.org/10.1016/j.msec.2019.110414.
[27] M. Patel, D.K. Dubey, S.P. Singh, Investigations into the role of water concentration on mechanical behavior and nanomechanics of Bombyx mori silk fibroin using molecular dynamics simulations, J. Mater. Sci. 55 (2020) 17019–17045, https://doi.org/10.1007/s10853-020-05249-3.
[28] W. Shen, Z. Tang, X. Wu, L. Pan, Y. Cheng, B. Hou, J. Song, W. Chen, B. Ji, D. Li, An atomistic model of silk protein network for studying the effect of pre-stretching on the mechanical performances of silks, Acta Mech. Sin. 38 (2022) 222013, https://doi.org/10.1007/s10409-022-22013-x.
[29] S. Keten, M.J. Buehler, Atomistic model of the spider silk nanostructure, Appl. Phys. Lett. 96 (15) (2010) 153701, https://doi.org/10.1063/1.3385388.
[30] S. Keten, M.J. Buehler, Nanostructure and molecular mechanics of spider dragline silk protein assemblies, J. R. Soc. Interface 7 (2010) 1709–1721, https://doi.org/10.1098/rsif.2010.0149.
[31] I. Krasnov, I. Diddens, N. Hauptmann, G. Helms, M. Ogurreck, T. Seydel, S. S. Funari, M. Müller, Mechanical properties of silk: interplay of deformation on macroscopic and molecular length scales, Phys. Rev. Lett. 100 (4) (2008) 048104, https://doi.org/10.1103/PhysRevLett.100.048104.
[32] J. Sirichaisit, V.L. Brookes, R.J. Young, F. Vollrath, Analysis of structure/property relationships in silkworm (Bombyx mori) and spider dragline (Nephila edulis) silks using Raman spectroscopy, Biomacromolecules 4 (2) (2003) 387–394, https://doi.org/10.1021/bm0256956.
[33] Q. Yang, W. Li, S.T. Stober, A.B. Burns, M. Gopinadhan, A. Martini, Molecular dynamics simulation of the stress-strain behavior of polyamide crystals, Macromolecules 54 (18) (2021) 8289–8302, https://doi.org/10.1021/acs.macromol.1c00974.
[34] S. Sockalingam, S.C. Chowdhury, J.W. Gillespie Jr, M. Keefe, Recent advances in modelling and experiments of Kevlar ballistic fibrils, fibers, yarns and flexible woven textile fabrics–a review, Text. Res. J. 87 (2017) 984–1010, https://doi.org/10.1177/0040517516646039.
[35] X. Liu, K.-Q. Zhang, Silk fiber-molecular formation mechanism, structure-property relationship and advanced applications, oligomerization of chemical and biological compounds, In. Tech. (2014), https://doi.org/10.5772/57611.
[36] A.P. Kiseleva, P.V. Krivoshapkin, E.F. Krivoshapkina, Recent advances in development of functional spider silk-based hybrid materials, Front. Chem. 8 (2020) 554, https://doi.org/10.3389/fchem.2020.00554.
[37] S.C. Chowdhury, S. Sockalingam, J.W. Gillespie, Molecular dynamics modeling of the effect of axial and transverse compression on the residual tensile properties of ballistic fiber, Fibers 5 (1) (2017) 7, https://doi.org/10.3390/fib5010007.
[38] R.E. Marsh, R.B. Corey, L. Pauling, An investigation of the structure of silk fibroin, Biochim. Biophys. Acta 16 (1955) 1–34, https://doi.org/10.1016/0006-3002(55)90178-5.
[39] K. Momma, F. Izumi, A three-dimensional visualization system for electronic and structural analysis, J. Appl. Cryst. 41 (3) (2008) 653–658, https://doi.org/10.1107/S0021889808012016.
[40] M.D. Hanwell, D.E. Curtis, D.C. Lonie, T. Vandermeersch, E. Zurek, G.R. Hutchison, Avogadro: an advanced semantic chemical editor, visualization, and analysis platform, J. Cheminf. 4 (2012) 17, https://doi.org/10.1186/1758-2946-4-17.
[41] B. Aksakal, Ü. Akdere, S.D. Günay, T. Çağın, Ç. Taşseven, Influence of repeating sequence on structural and thermal stability of crystalline domain of bombyx mori silk fibroin, Mater. Res. Express 6 (12) (2008) 53–56, https://doi.org/10.1088/2053-1591/ab6548.
[42] B. Hess, C. Kutzner, D. Van Der Spoel, E. Lindahl, GROMACS 4: algorithms for highly efficient, load-balanced, and scalable molecular simulation, J. Chem. Theory Comput. 4 (3) (2008) 435–447, https://doi.org/10.1021/ct700301q.
[43] B.R. Brooks, C.L. Brooks 3rd, A.D. Mackerell Jr, L. Nilsson, R.J. Petrella, B. Roux, Y. Won, G. Archontis, C. Bartels, S. Boresch, A. Caflisch, L. Caves, Q. Cui, A. R. Dinner, M. Feig, S. Fischer, J. Gao, M. Hodoscek, W. Im, K. Kuczera, T. Lazaridis, J. Ma, V. Ovchinnikov, E. Paci, R.W. Pastor, C.B. Post, J.Z. Pu, M. Schaefer, B. Tidor, R.M. Venable, H.L. Woodcock, X. Wu, W. Yang, D.M. York, M. Karplus, CHARMM: the biomolecular simulation program, J. Comput. Chem. 30 (10) (2009) 1545–1614, https://doi.org/10.1002/jcc.21287.
[44] B. Mercer, E. Zywicz, P. Papadopoulos, A molecular dynamics-based analysis of the influence of strain-rate and temperature on the mechanical strength of PPTA crystallites, Polymer 129 (2017) 92–104, https://doi.org/10.1016/j.polymer.2017.09.037.
[45] K. Nakamae, T. Nishino, Y. Gotoh, R. Matsui, M. Nagura, Temperature dependence of the elastic modulus of the crystalline regions of poly(p-phenylene benzobisthiazole), Polymer 40 (16) (1999) 4629–4634, https://doi.org/10.1016/S0032-3861(99)00073-7.
[46] T. Kurita, Y. Fukuda, M. Takahashi, Y. Sasanuma, Crystalline moduli of polymers, evaluated from density functional theory calculations under periodic boundary conditions, ACS Omega 3 (5) (2018) 4824–4835, https://doi.org/10.1021/acsomega.8b00506.